2026 IEEE International Conference on Robotics and Automation (ICRA 2026)
June 1-5, 2026. Vienna, Austria

PERAL: Perception-Aware Motion Control for Passive LiDAR Excitation in Spherical Robots

Shenghai Yuan*, *Member, IEEE*, Jason Wai Hao Yee*,
Weixiang Guo, Zhongyuan Liu, Thien-Minh Nguyen, and Lihua Xie†, *Fellow, IEEE*

***Abstract*— Autonomous mobile robots increasingly rely on LiDAR–IMU odometry for navigation and mapping, yet horizontally mounted LiDARs often provide poor near-ground coverage, while alternative configurations risk geometric degeneracy. To address this, we present PERAL, a perception-aware spherical robot that enhances LiDAR viewpoint diversity through passive self-excitation, without dedicated scanning actuators. By exploiting the coupling between internal differential-drive motion and shell attitude, PERAL naturally induces mild sensor rocking during locomotion, enriching vertical observations. In controlled trials over comparable traveled distances, PERAL achieves (75.7%) coverage, substantially outperforming a fixed-horizontal differential-drive baseline (15.5%) and approaching a quadruped platform with a bottom-mounted rotating LiDAR (84.7%). Additional experiments demonstrate consistent path-following behavior across two shell sizes, reliable operation in both manual and autonomous modes, and successful traversal of a 15° slope. These results suggest that passive self-excitation offers an effective and lightweight alternative to active LiDAR actuation for improving near-ground perceptual coverage on compact mobile robots. Design and code are available at `https://github.com/snakehaihai/PERAL_robot_design`.**

I. INTRODUCTION

LiDAR-based perception [1] supports mapping [2], localization [3], and navigation [4] in mobile robotics [5]. Many critical cues lie near the ground [6], for both safe motion and ground-level target detection, yet common horizontal LiDAR mounting yields sparse near-ground coverage and blind zones in flat or feature-sparse scenes [7]. As lightweight sensors such as the MID360 become standard on compact robots, improving near-ground coverage increasingly becomes a design trade-off between sensor motion and sensing density, especially in open or weakly structured spaces.

Existing approaches improve ground coverage in several ways. Actuated excitation, used in systems such as PULSAR [8], UA-MPC [9], αLiDAR [10] and FLARE [11], rotates the LiDAR to expand the effective vertical field-of-view, but adds actuation hardware, control complexity, and power draw. Static tilted mounting [12] is simple and low cost, but trades off horizontal scanning uniformity and can reduce robustness in long, repetitive structures [13]. Alternatively, high-density LiDARs (e.g., Ouster-class sensors) provide denser near-ground coverage [13], but their cost and power footprint remain prohibitive for compact platforms.

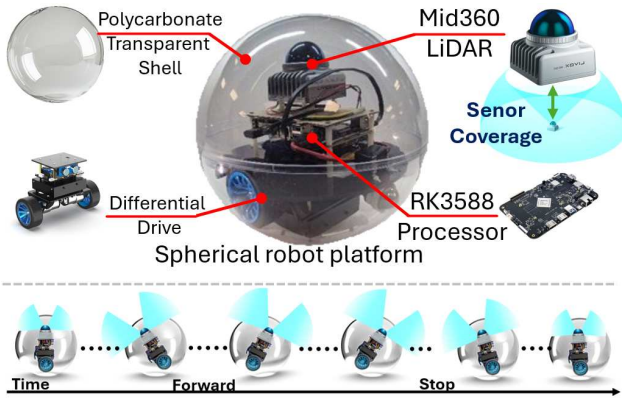

Fig. 1. Hardware and perception architecture of the spherical robot (top) and its rolling motion over time (bottom). The internal wheel drive induces passive pitch excitation during rolling, which excites the top-mounted MID360 LiDAR and increases near-ground coverage without scanning actuation, especially during acceleration and braking on uneven ground.

The core **challenge** is to increase near-ground coverage *without* sacrificing compactness, introducing dedicated scanning actuators, or incurring large cost, weight, and power overhead.

To address this challenge, we present **PERAL**, a passive LiDAR excitation approach enabled by the intrinsic rolling motion of a spherical mobile robot. The robot drives through an internal differential-drive mechanism enclosed by a spherical shell. The resulting drive–shell coupled with ground contact naturally induces small, non-periodic LiDAR attitude variations during locomotion. These passive oscillations broaden the vertical scan distribution and improve near-ground coverage without additional actuators or dedicated scanning hardware. We validate the approach on a compact real robot through local coverage comparison, path-following tests, and field demonstrations. The contributions of this work are:

- We show that passive LiDAR excitation can arise naturally in spherical locomotion: drive–shell coupling and contact effects induce small, non-periodic attitude variations that improve scan diversity without dedicated scanning actuation.
- We provide a compact motion–perception rationale that relates internal wheel actuation, shell attitude variation,

*Equal contribution. †Corresponding author.

This work was supported by the Centre for Advanced Robotics Technology Innovation (CARTIN) and the National Research Foundation (NRF), Singapore. This work was also supported by Chery International under its collaboration projects with Nanyang Technological University (NTU).

Shenghai Yuan, Jason Wai Hao Yee, Weixiang Guo, Zhongyuan Liu, and Lihua Xie are with CARTIN and School of Electrical and Electronic Engineering, NTU, 50 Nanyang Avenue, Singapore. Thien-Minh Nguyen is with The University of Queensland (UQ), Australia.

Emails: {shyuan, elhxie}@ntu.edu.sg; thienminh.nguyen@uq.edu.au.

and LiDAR viewing direction, explaining how rolling motion reshapes vertical sensing coverage.
- We validate the approach on real spherical robots with quantitative local coverage experiments, and further demonstrate operation across different shell sizes, under both manual and autonomous modes, and on a 15° slope.

Remark: Throughout this paper, we use *scan diversity* to describe motion-induced variation in LiDAR orientation that enables more reliable observation of structures such as near-ground regions and vertical surfaces. This notion is distinct from classical EKF observability: we do not claim changes in Jacobian rank or formal persistent excitation. Instead, our focus is on improved point coverage and spatial distribution, which leads to better local coverage in the experiments.

II. Related Work

A. LiDAR-Based SLAM and Perception Limitations

LiDAR-based simultaneous localization [14] and mapping (SLAM) [15]–[21] has advanced rapidly with the emergence of tightly coupled LiDAR–inertial odometry (LIO) frameworks [22], [23]. Representative works include *FAST-LIO* and its successors [24], [25], which exploit iterated Kalman filtering and direct raw point registration for efficient and robust state estimation. *Swarm-LIO* [26] extends this paradigm to multi-UAV scenarios, enabling decentralized odometry under bandwidth and scalability constraints. More recently, *IG-LIO* [27] extends this line of work to large-scale and long-duration scenarios, leveraging an incremental GICP formulation for tightly coupled LiDAR–IMU odometry. Beyond pure LiDAR–IMU systems, multi-modal approaches such as *R3LIVE* [28] introduce visual and color cues for improved perceptual richness, while *BEV-LIO(LC)* [29] leverages bird's-eye-view image priors to facilitate loop closure. Similarly, *Kenji et al.* [30] employs GPU-accelerated generalized ICP factors for scalable scan matching, and *LiTAMIN2* [31] achieves lightweight mapping through KL-divergence based geometric approximations. Finally, *Adaptive-LIO* [32] demonstrates that environment-aware adaptation can further stabilize odometry across diverse scenes.

Despite these advances, a fundamental limitation persists: horizontally mounted LiDARs often provide insufficient vertical coverage on compact platforms. In feature-sparse settings, such as corridors, open fields, or smoke-filled spaces, this results in degraded observability, incomplete maps, and fragile loop closures. While recent algorithms improve efficiency and robustness, they cannot fully compensate for sensing blind spots. This motivates motion-induced strategies that enrich LiDAR coverage.

B. Active Excitation Mechanisms for Observability

To overcome the sensing blind spots of horizontally mounted LiDARs, a number of works have pursued *active excitation*, where additional motions or actuators are introduced to enrich scan diversity and improve state observability. Representative examples include *PULSAR* [8], a self-rotating, single-actuated UAV that continuously spins to extend the sensor field of view for navigation and obstacle detection. To support robust state estimation under such aggressive self-rotation, *PULSAR* employs *Point-LIO* [33], a high-bandwidth LiDAR–IMU odometry method designed for rapid motion and low-latency sensor fusion. Another line of work incorporates active control strategies. For instance, *UA-MPC* [9] formulates LiDAR odometry within an uncertainty-aware model predictive control framework, where actuator-driven oscillations explicitly increase vertical coverage. In parallel, calibration-oriented efforts such as *LiMo-Calib* [34] explore motorized LiDAR setups on quadruped robots, enabling panoramic 3D sensing through deliberate rotational excitation. While effective, these active excitation methods inevitably introduce drawbacks: they require additional actuators [35] or control complexity, increase power consumption, and often demand precise calibration or synchronization. Such trade-offs limit their practicality for lightweight and energy-constrained robotic platforms.

C. Persistent Excitation and Observability

The concept of *persistent excitation* (PE) is fundamental for ensuring observability and stability in estimation and control. Recent theoretical studies formalize explicit PE requirements for observer stability [36] and analyze global observability conditions in nonholonomic robotic systems [37]–[43]. In multi-robot and swarm scenarios, it has been shown that persistently exciting relative motions enable accurate adaptive localization and stable formation control [44]. Related works on target encirclement further exploit motion diversity to improve robustness against noise and environmental complexity [45]–[47]. These results highlight that perception and control are tightly coupled, and that observability can be actively enhanced by introducing excitation.

However, enforcing PE often requires deliberate path design or additional actuation, which may be costly for small, resource-constrained robots. This motivates the exploration of *passive motion coupling*, where natural dynamics—such as rolling, braking, and turning—provide sufficient excitation to diversify LiDAR scans and enhance near-ground observability without dedicated mechanisms.

Motivation. Koide et al. [48] developed a globally consistent LiDAR-inertial mapping system with GPU-accelerated registration. In their demonstration of a transparent passive spherical robot carrying a LiDAR sensor, external perturbations such as kicking induce additional rocking and attitude variation, which appears to improve scene coverage. This observation motivates our work: rather than introducing dedicated sensor actuation, we study whether naturally induced rocking can be systematically leveraged to enhance near-ground perception. To the best of our knowledge, this specific idea has not been explicitly explored in prior work. Our goal is to examine its practical feasibility and to characterize both its potential benefits and its limitations.

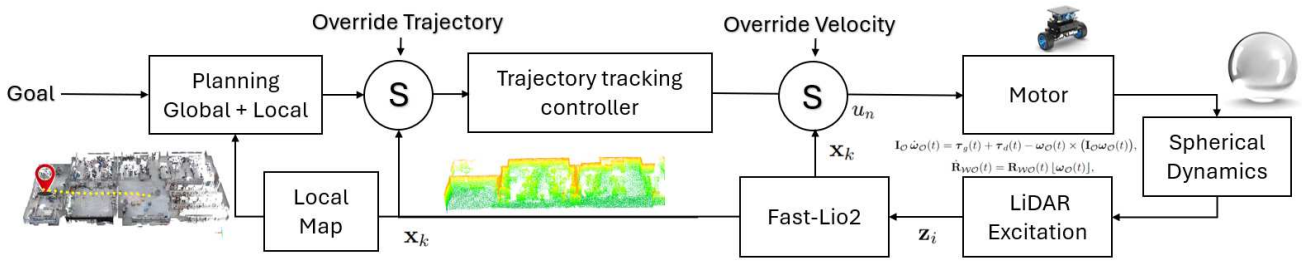

Fig. 2. System architecture of the spherical robot with multi-mode control inputs. The framework supports goal-driven planning, direct path input, and manual velocity overrides, all unified through a path tracking controller with oscillation shaping. The resulting motion naturally excites the LiDAR for enhanced perception without additional actuation.

III. Proposed Method

A. System Overview

As shown in Fig. 2, the spherical robot navigates either toward assigned goals via global–local planning or along predefined trajectories using its internal differential-drive unit. Acceleration, braking, and turning induce small pitch–roll oscillations to the spherical robot, tilting the horizontally mounted LiDAR and passively diversifying scan directions without extra actuation. LiDAR–IMU fusion is performed using the discrete-time FAST-LIO pipeline, with LiDAR frames processed at their acquisition rate and IMU preintegration in between. Hardware, calibration, and baseline settings are detailed in Sec. IV.

B. Problem Formulation

Frames and Extrinsics. Let $\{\mathcal{W}\}$ be the world frame, $\{\mathcal{O}\}$ the outer-shell frame at the sphere center, $\{\mathcal{I}\}$ the internal drive frame, and $\{\mathcal{L}\}$ the LiDAR frame. The shell pose is

$$\mathbf{T}_{\mathcal{WO}}(t) = \begin{bmatrix} \mathbf{R}_{\mathcal{WO}}(t) & \mathbf{p}_{\mathcal{WO}}(t) \\ \mathbf{0}^\top & 1 \end{bmatrix}. \tag{1}$$

The extrinsic calibration is

$$\mathbf{T}_{\mathcal{OL}} = \begin{bmatrix} \mathbf{R}_{\mathcal{OL}} & \mathbf{p}_{\mathcal{OL}} \\ \mathbf{0}^\top & 1 \end{bmatrix}, \mathbf{T}_{\mathcal{OI}}(t) = \begin{bmatrix} \mathbf{R}_{\mathcal{OI}}(t) & \mathbf{p}_{\mathcal{OI}}(t) \\ \mathbf{0}^\top & 1 \end{bmatrix}. \tag{2}$$

State and Input. We define the platform state $\mathbf{x}(t) = [\mathbf{p}_{\mathcal{WO}}(t), \mathbf{v}(t), \mathbf{R}_{\mathcal{WO}}(t), \mathbf{b}_a(t), \mathbf{b}_\omega(t)]$, where $\mathbf{p}_{\mathcal{WO}}$ is the position of $\{\mathcal{O}\}$ in $\{\mathcal{W}\}$, $\mathbf{v}$ is the linear velocity, $\mathbf{R}_{\mathcal{WO}} \in SO(3)$ is the orientation, and $\mathbf{b}_a, \mathbf{b}_\omega$ are IMU biases. The internal differential-drive input is $\mathbf{u}(t) = [u_L(t), u_R(t)]^\top$. With wheel radius r and track width d, the drive-frame twist is

$$\begin{aligned} \mathbf{v}_{\mathcal{I}}(t) &= \begin{bmatrix} \frac{r}{2}\big(u_L(t) + u_R(t)\big) \\ 0 \\ 0 \end{bmatrix}, \\ \boldsymbol{\omega}_{\mathcal{I}}(t) &= \begin{bmatrix} 0 \\ 0 \\ \frac{r}{d}\big(u_R(t) - u_L(t)\big) \end{bmatrix}. \end{aligned} \tag{3}$$

An equivalent planar wheel-rate form commonly used in spherical-robot modeling is provided in the appendix for reference.

Drive–Shell Coupling. We use a kinematic approximation to relate the internal drive motion to the shell motion. Assuming quasi-static contact and no slip at the drive–shell interface, the shell translation is opposite to the internal-drive translation expressed in $\{\mathcal{O}\}$:

$$\mathbf{v}_{\mathcal{O}}^{\mathcal{O}}(t) \approx -\,\mathbf{R}_{\mathcal{OI}}(t)\,\mathbf{v}_{\mathcal{I}}^{\mathcal{I}}(t). \tag{4}$$

For an ideal rolling shell of radius R_s, the no-slip constraint at the ground contact implies

$$\mathbf{v}_{\mathcal{O}}^{\mathcal{O}}(t) \approx \boldsymbol{\omega}_{\mathcal{O}}(t) \times \mathbf{r}_c, \qquad \|\mathbf{r}_c\| = R_s, \tag{5}$$

which induces an angular velocity $\boldsymbol{\omega}_{\mathcal{O}}(t)$ consistent with the instantaneous contact vector $\mathbf{r}_c$. The shell pose evolves as

$$\dot{\mathbf{p}}_{\mathcal{WO}}(t) = \mathbf{R}_{\mathcal{WO}}(t)\,\mathbf{v}_{\mathcal{O}}^{\mathcal{O}}(t), \dot{\mathbf{R}}_{\mathcal{WO}}(t) = \mathbf{R}_{\mathcal{WO}}(t)\,\lfloor\boldsymbol{\omega}_{\mathcal{O}}(t)\rfloor. \tag{6}$$

In practice, slip and terrain irregularities may violate (4)–(5), so we use them as a physical rationale rather than hard constraints.

Remark. By default, our implementation for the current hardware design does not inject an explicit periodic excitation for the two built prototypes. However, if the ball shell is much bigger than the internal robot, additional excitations may be needed.

C. Passive LiDAR Excitation via Spherical Dynamics

Let $\mathbf{u}(t) = [u_L(t), u_R(t)]^\top$ denote wheel angular velocities. The internal motion shifts the instantaneous center of mass in $\{\mathcal{O}\}$, producing an offset $\mathbf{c}_{\mathcal{O}}(t)$ and the corresponding gravity/contact torque

$$\boldsymbol{\tau}_g(t) = \mathbf{c}_{\mathcal{O}}(t) \times m\,\mathbf{g}_{\mathcal{O}}. \tag{7}$$

The shell attitude follows the rigid-body dynamics

$$\mathbf{I}_{\mathcal{O}}\,\dot{\boldsymbol{\omega}}_{\mathcal{O}}(t) = \boldsymbol{\tau}_g(t) + \boldsymbol{\tau}_d(t) - \boldsymbol{\omega}_{\mathcal{O}}(t) \times \big(\mathbf{I}_{\mathcal{O}}\boldsymbol{\omega}_{\mathcal{O}}(t)\big), \tag{8}$$

$$\dot{\mathbf{R}}_{\mathcal{WO}}(t) = \mathbf{R}_{\mathcal{WO}}(t)\,\lfloor\boldsymbol{\omega}_{\mathcal{O}}(t)\rfloor, \tag{9}$$

where $\boldsymbol{\tau}_d(t)$ aggregates the drive-induced contact and friction effects and is not required in closed form in our analysis. With fixed extrinsics $\mathbf{T}_{\mathcal{OL}}$, the LiDAR pose is

$$\mathbf{T}_{\mathcal{WL}}(t) = \mathbf{T}_{\mathcal{WO}}(t)\,\mathbf{T}_{\mathcal{OL}}. \tag{10}$$

A world point $\mathbf{p}_i^{\mathcal{W}}$ yields the measurement

$$\mathbf{z}_i(t) = \pi\big(\mathbf{T}_{\mathcal{WL}}(t)^{-1}\mathbf{p}_i^{\mathcal{W}}\big) + \mathbf{n}_i(t), \tag{11}$$

so attitude variations in $\mathbf{R}_{\mathcal{WO}}(t)$ diversify scan directions and intermittently expose near-ground regions without dedicated scanning actuation.

D. Discrete-Time State Estimation

Our FAST-LIO backend runs in discrete time at LiDAR timestamps t_k. At frame k, the state

$$\mathbf{x}_k = [\,\mathbf{p}_k,\, \mathbf{v}_k,\, \mathbf{R}_k,\, \mathbf{b}_{a,k},\, \mathbf{b}_{\omega,k}\,]$$

contains position, velocity, orientation, and IMU biases. IMU measurements are preintegrated [25] between t_k and t_{k+1} to form the residual $\mathbf{r}_{I,k,k+1}$. Each LiDAR scan $\mathcal{Z}_k$ is aligned to the local map using FAST-LIO's scan-to-map residual $\mathbf{r}_{L,k}$, which is formed from local geometric constraints on selected map features [25]. The backend minimizes

$$\min_{\{\mathbf{x}_k\}} \sum_k \|\mathbf{r}_{L,k}\|^2_{\Sigma_L} + \|\mathbf{r}_{I,k,k+1}\|^2_{\Sigma_I}.$$

Implementation details follow the referenced FAST-LIO pipeline and our released codebase.

E. Path Following and Low-level Control

Let $\mathbf{x}_k^E$ denote the LIO estimate at LiDAR frame k and $\mathbf{x}_n^*$ the reference at control cycle n. Between LiDAR updates, $\mathbf{x}_k^E$ is held constant or interpolated to obtain $\mathbf{x}_n^C$. The tracking error is

$$\mathbf{e}_n = \mathbf{x}_n^* - \mathbf{x}_n^C.$$

A PID controller generates the nominal velocity command $(\bar{v}_n, \bar{\omega}_n) = \Pi(\mathbf{e}_n)$, where $\Pi(\cdot)$ denotes the tracking law.

To maintain scan diversity only when passive rocking becomes insufficient, we optionally augment the nominal linear command by

$$v_n = \bar{v}_n + A_e \sin(2\pi f_e n T_c), \qquad \omega_n = \bar{\omega}_n, \tag{12}$$

where $A_e \geq 0$ is a heuristic excitation amplitude, f_e is the excitation frequency, and T_c is the control period. This term is not derived from a formal stability or convergence analysis, and we do not claim that (12) alone provides closed-loop guarantees. Let O_{cg} and O_{geo} denote the internal mass center and the geometric center of the spherical shell, and define $\delta := \|O_{\mathrm{cg}} - O_{\mathrm{geo}}\|$. Empirically, when δ is small, the coupled sphere-drive system is more prone to natural attitude oscillation (See Fig. 4, the smaller ball has more oscillations), so passive scan excitation is typically sufficient and one may set $A_e = 0$. When δ is larger, which typically corresponds to a larger shell with a relatively compact internal drive, the local tangent space becomes effectively flatter and the motion approaches planar rolling. In this regime, passive rocking weakens and a small $A_e > 0$ may be introduced to recover comparable viewpoint variation for local perception. But so far, this is only set for extreme cases in simulation. Thus, (12) should be interpreted as a scale-dependent heuristic compensation term rather than an optimal control law. Unless otherwise specified, all real-world experiments reported in this paper use $A_e = 0$. The wheel angular velocities follow the standard differential-drive map and we form $\mathbf{u}_n = [u_L(n),\, u_R(n)]^\top$ for execution on the internal drive,

$$u_L(n) = \frac{1}{r}\left(v_n - \frac{d}{2}\,\omega_n\right), \quad u_R(n) = \frac{1}{r}\left(v_n + \frac{d}{2}\,\omega_n\right). \tag{13}$$

IV. Experiments

A. Experimental Setup

Our experimental platform consists of two custom-built spherical mobile robots with internal differential-drive mechanisms, each equipped with a DJI Livox Mid-360 LiDAR and an onboard IMU. A LubanCat RK3588 single-board computer running ROS 2 performs onboard data acquisition and processing. The two robot variants have outer diameters of 25 cm and 16 cm, respectively. The tests were conducted in three representative environments:

- **Indoor laboratory:** cluttered space with desks, chairs, and equipment.
- **Corridor:** long, narrow passages with sparse geometric features.
- **Tactical training center:** environment with obstacles and a sloped floor to evaluate operation on inclined terrain.

Conducting hardware-level comparisons across heterogeneous robot platforms is inherently challenging because fairness, feasibility, and platform-specific design constraints must all be balanced. Since our primary goal is to compare system-level sensing and mapping behavior rather than controller-specific optimality, we benchmark three representative configurations: (i) a differential-Wheel drive robot (Diff-W) with a fixed horizontal LiDAR (FHL), representative of common compact mobile mapping setups [49]–[51]; (ii) a quadruped robot (Quad) with a bottom-mounted spinning LiDAR and onboard odometry (SPIN); and (iii) the proposed PERAL spherical robot with self-excited LiDAR sensing (SEL). Although we initially considered a mecanum-wheel platform, we ultimately adopt a differential-drive baseline for the controlled comparison, since plastic mecanum platforms within a comparable cost range exhibited less stable motion and less reliable path following, which would otherwise confound the sensing and mapping evaluation.

B. Evaluation Metrics

Our evaluation includes quantitative and qualitative measures:

- **Path-Following Performance:** mean deviation from a predefined reference path when the robot is manually driven to follow a target trajectory shape. We report both the absolute error and the signed error, where the sign is defined by the local tangent and normal of the reference path, to explicitly visualize zero-crossings when the executed trajectory intersects the reference path.

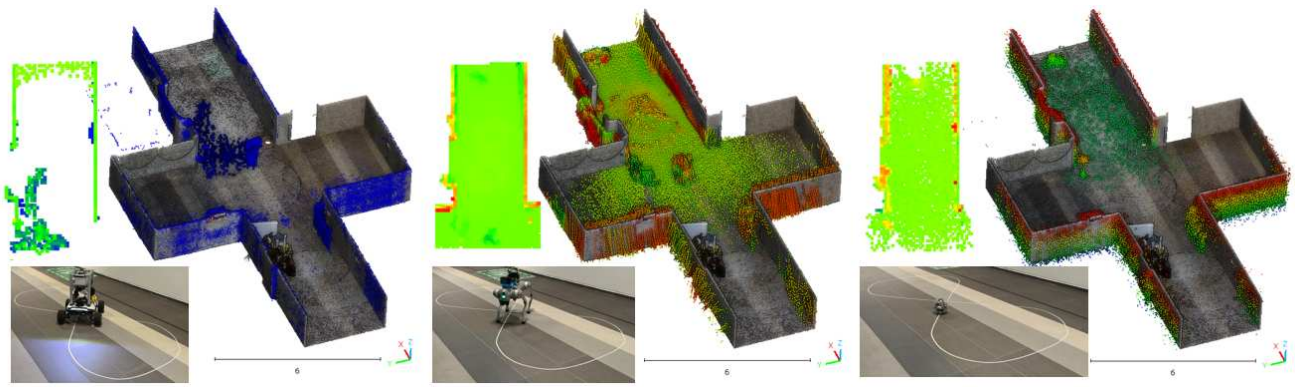

Fig. 3. System-level map reconstruction comparison across three robot platforms in the same corridor environment. For fairness, all platforms are manually driven along the same short figure-eight trajectory with comparable travel distance. From left to right: a differential-drive robot with a fixed horizontal LiDAR, a quadruped robot, and the proposed PERAL spherical robot.

TABLE I

ILLUSTRATIVE SYSTEM-LEVEL COMPARISON ACROSS REPRESENTATIVE ROBOT PLATFORMS.

Platform	C	**Power**	**Cost**	**Weight**	**Size** (cm)
Diff-W FHL	15.5%	140 W	3.8k$	26 kg	$61 * 58 * 72$
Quad SPIN	**84.7**%	160 W	13k$	16 kg	$70 * 31 * 60$
PERAL SEL	75.7%	**22** W	**2.1k**$	**1.8** kg	Small $\varnothing$ 16 Large $\varnothing$ 25

Note: This table is intended as an illustrative system-level comparison rather than a standardized benchmark. Most values are taken from publicly available specifications, with a small portion based on our direct measurements or engineering estimates when official data are unavailable. The coverage value C is obtained from short-range local trials in which each robot traverses a comparable path segment within a small area with voxel size 0.1 and 2m radius. To reduce controller-dependent effects, the reported coverage comparison is based on manually driven trials and should be interpreted as a practical comparison of integrated sensing configurations rather than an isolated evaluation of a single sensing mechanism.

- **Map Coverage:** Map coverage C is computed as

$$C = \frac{|\mathcal{V}_{\text{ref}} \cap \mathcal{V}_{\text{est}}|}{|\mathcal{V}_{\text{ref}}|},$$

  where $\mathcal{V}_{\text{ref}}$ and $\mathcal{V}_{\text{est}}$ denote the occupied voxels in the Leica reference map and the reconstructed map, respectively.
- **System efficiency:** comparison of power, cost, weight, and volume across platforms (see Tab. I).

C. Experimental Procedure

All three platforms are manually driven to traverse an identical Figure-8 route to avoid confounds from controller tuning and to enable a behavior-matched comparison. Robots are operated at comparable speeds (0.2–0.6 m/s) while LiDAR and IMU data are recorded. For the two DIY platforms, we use the same LiDAR–IMU unit and process measurements with an identical FAST-LIO2 pipeline for odometry and mapping. For the Unitree Go2, we use its bottom-mounted rotating LiDAR and Point-LIO for odometry and mapping. In addition, we conduct autonomous circular and oval tracking tests on PERAL using our MPC+PID controller to stress-test tracking under higher curvature and to characterize its performance envelope.

Path-Following Performance is evaluated using two reference trajectories:

- **Circle**: a circle ($R = 0.5$ m), evaluating steady turns.
- **Oval:** an ellipse (1×2 m), evaluating sharp turns.

We compute the mean absolute tracking error as the shortest Euclidean distance from each estimated position to the reference path, with samples aligned by normalized time to account for different traversal speeds at different size (See Fig. 4).

V. RESULTS AND DISCUSSION

A. System-Level Comparison

Tab. I summarizes the trade-offs between local coverage and system efficiency. The fixed-horizontal differential-drive platform offers low cost and low power, but its scene coverage remains very limited in short-range figure-8 motion. The quadruped robot achieves the highest local coverage, but at substantially higher cost, weight, and power. PERAL provides a favorable middle ground: within a limited travel distance, it attains good coverage while maintaining a compact form factor (1.8 kg for both $\varnothing 16/25$ cm shell), modest power consumption (22 W), and relatively low system cost. These results suggest that passive self-excitation is an effective way to improve local perceptual coverage without the added complexity of dedicated active scanning hardware.

B. Short-Range Coverage Comparison

As shown in Fig. 3, we evaluate short-range coverage under figure-8 motion, where each robot traverses a comparable local path segment. Rather than emphasizing global mapping over long distances, this experiment focuses on how much nearby scene structure can be observed within a limited travel distance. Coverage differs markedly across platforms. In the ± 2 m radius range, which corresponds to the typical spatial extent used for local planning of the ball robot, the fixed-horizontal differential-drive baseline achieves

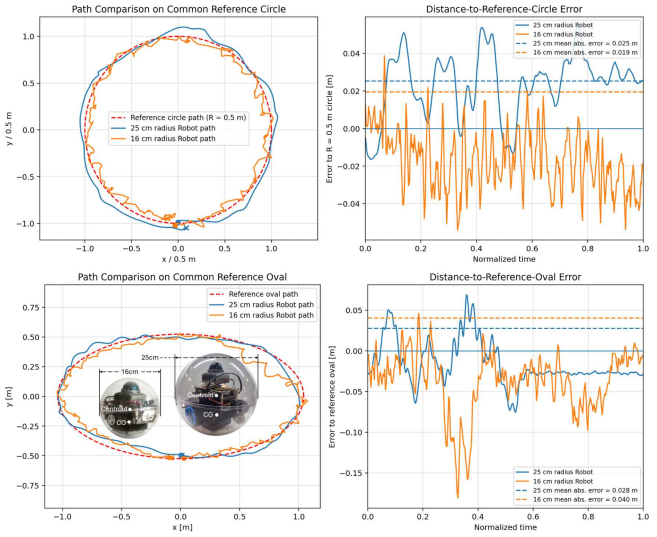

Fig. 4. Autonomous path following of PERAL on circular and oval reference paths using an MPC+PID controller. The commanded speed setpoint is 0.2 m/s. We compare two spherical robot configurations with different shell diameters ⌀ (25 cm and 16 cm). For both reference paths, the path-following behavior and error magnitude remain broadly similar across the two robot sizes, indicating that the control framework maintains comparable tracking performance under different spherical dimensions. The error is computed from raw FAST-LIO2 odometry as the signed shortest distance to the reference path, with the sign determined by the local path tangent.

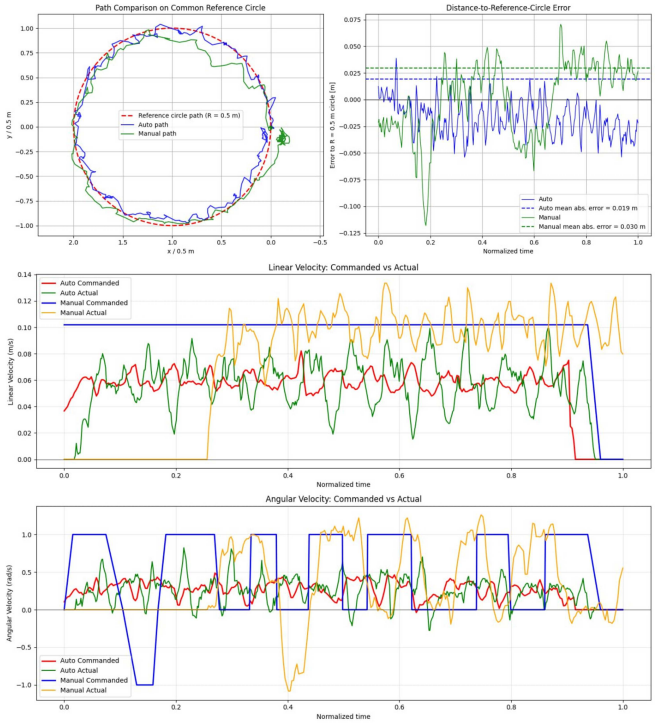

Fig. 5. Autonomous versus manual circular path following on a common reference circle for the 16 cm spherical robot. The top row shows trajectory overlap and signed distance-to-reference error, while the bottom rows compare commanded and actual linear/angular velocities. Autonomous control achieves a smaller mean absolute tracking error (0.019 m) than manual control (0.030 m) and exhibits more consistent motion execution. Both control methods shows similar vibrations effects.

only ∼15.5% coverage, whereas PERAL reaches ∼75.7%. The quadruped platform with a bottom-mounted rotating LiDAR achieves the highest coverage of ∼84.7%. In the more restrictive ± 0.5 m range, which reflects the immediately traversable region, the wheeled robot, quadruped, and PERAL achieve coverage rates of ∼9%, 100%, and ∼96%, respectively. These results indicate that PERAL substantially improves both planning-relevant local map completeness and immediate near-ground observability over the fixed-horizontal wheeled baseline.

C. Path-Following and Passive Oscillation Analysis

We compare path-following performance across control modes and platform scales as shown in Fig 4 and Fig 5. Overall, the tracking errors remain similar across the tested conditions: manual and autonomous operation achieve comparable path-following accuracy, and the ⌀16cm and ⌀25cm spherical robots also show similar errors under autonomous control. The more noticeable difference lies in the motion profile during traversal. The smaller sphere exhibits stronger oscillatory rocking, whereas the larger sphere moves more smoothly with weaker passive oscillation. This indicates that, for a fixed internal drive configuration, increasing the outer shell size reduces the magnitude of passive self-excitation. As a result, if the sphere size continues to increase while the internal robot remains unchanged, the platform will gradually approach near-horizontal motion with little natural oscillation, and additional external excitation may be required to maintain comparable viewpoint variation for perception.

D. Slope Crossing Capability

To further validate mobility, we tested the PERAL robot on an inclined ramp inside the tactical training center (Fig. 6). The robot successfully ascended a slope of approximately 15° without loss of stability or slippage. This demonstrates that the passive self-excitation mechanism does not hinder basic locomotion performance, and the spherical design preserves sufficient ground traction to handle moderate inclines. Such capability is important for mixed indoor–outdoor or semi-structured environments, where uneven terrain or ramps are common.

E. Ground-Level Target Detection and Applications

We further demonstrate ground-level target detection by placing a human-sized dummy in the tactical training center and commanding the robot to navigate along a loop path around it (see Fig. 6). Due to its low chassis and passive self-excitation, *PERAL* can capture floor-level structures and low-height returns from the dummy during motion, and these observations are directly incorporated into the SLAM map without any dedicated detection module. As a result, the dummy becomes visible in the reconstructed map as local occupied structure near the ground. This capability is particularly relevant in smoky or visibility-degraded environments, where perception at higher elevations may be limited while the ground region remains partially observable. In

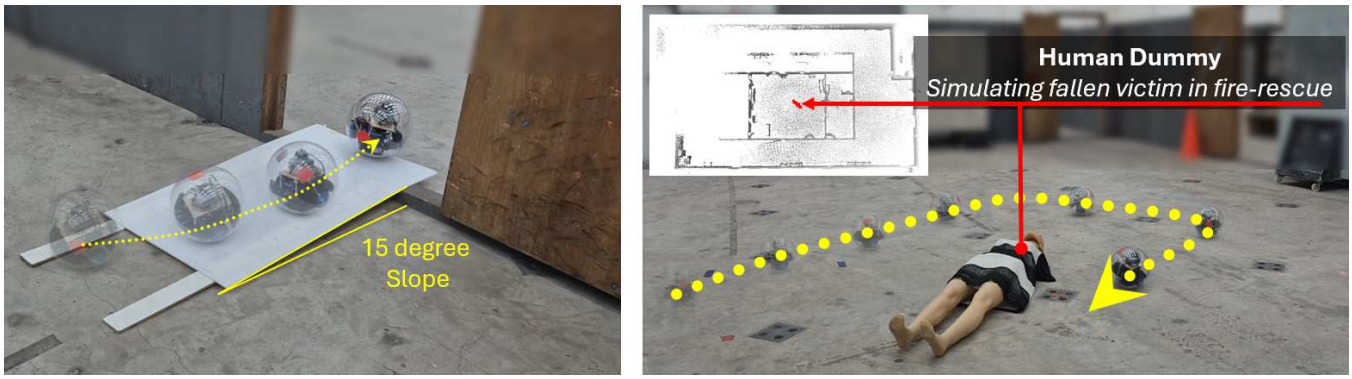

Fig. 6. Tactical training center experiments with ⌀25cm robot controlled manually. **Left:** PERAL climbing a $\sim 15^{\circ}$ ramp, demonstrating stable locomotion on inclined terrain. **Right:** Near-ground human-dummy detection scenario (simulating a fallen victim in fire-rescue); the yellow trajectory indicates the robot path, and the inset shows the corresponding SLAM map/reconstruction, highlighting improved observability of low-height structures enabled by passive LiDAR excitation.

such scenarios, improved near-ground perception can support victim localization and enhance situational awareness for search-and-rescue tasks.

Limitations. The proposed passive excitation should not be interpreted as satisfying persistent excitation in the strict control-theoretic sense, and we do not claim formal stability or convergence guarantees for the underlying state estimation process based on standard PE analysis. Instead, the observed improvements in scan diversity and coverage are supported by empirical results from the presented experiments.

A key reason is that the drive–shell interaction is difficult to model accurately in practice. Our analysis adopts an idealized rolling approximation, while the actual platform behavior can be affected by internal friction, wheel–shell slip, ground slip, and uneven or compliant terrain. These effects make the induced attitude variation difficult to predict precisely and limit the extent to which the excitation can be characterized analytically. The refraction and scattering through the transparent shell may introduce extra sensing artifacts, which can make the resulting maps slightly noisier than those obtained without the shell, as illustrated in Fig. 3.

In addition, the passive excitation depends on the locomotion and tends to diminish during prolonged constant-velocity motion or stationary operation. Therefore, the current mechanism should be viewed as a heuristic source of useful viewpoint variation rather than a guaranteed observability condition. Future work will investigate more formal observability analysis and hybrid passive–active designs that remain effective across a wider range of operating conditions.

VI. Conclusion

This paper presents a passive LiDAR excitation strategy for spherical mobile robots, leveraging the platform's inherent rocking motion to improve near-ground perception without additional scanning actuators. By exploiting locomotion-induced attitude oscillations, the approach causes intermittent reorientation of the LiDAR scanning plane and enables observation of ground regions that are difficult to capture with a fixed horizontal configuration.

Experiments in laboratory, corridor, and tactical training center environments show that the proposed approach alleviates near-ground sensing blind spots, enriches low-height map structure, and consistently improves local near-ground coverage relative to a fixed-horizontal baseline, while preserving mechanical simplicity. These results suggest that passive excitation offers a practical low-complexity sensing alternative for compact mobile platforms.

Future work will focus on developing a more rigorous characterization of the perception and mapping effects induced by passive excitation, bridging the gap between empirical findings and formal analysis. In parallel, we plan to explore reinforcement learning [52] and other data-driven optimization strategies to tune motion parameters or plan excitation-aware trajectories while preserving the actuator-light nature of the platform.

Acknowledgments

This work was developed with assistance from OpenAI's GPT-4. The system was used for (i) generating and refining code for the integration of robot functions, including autonomous control modules, and (ii) drafting and editing sections of the manuscript. All AI-generated content was reviewed and verified by the authors.

References

[1] J. Hou, P. Yang, X. Dai, T. Qin, and F. Lyu, "Enhancing cooperative lidar-based perception accuracy in vehicular edge networks," *IEEE Trans. Intell. Transp. Syst.*, 2025.

[2] X. Zhong, Y. Pan, C. Stachniss, and J. Behley, "3d lidar mapping in dynamic environments using a 4d implicit neural representation," in *Proc. IEEE/CVF Conf. Comput. Vis. Pattern Recogn. (CVPR)*, 2024.

[3] S. Yuan, H. Wang, and L. Xie, "Survey on localization systems and algorithms for unmanned systems," *Unmanned Syst.*, 2021.

[4] H. Yin, X. Xu, S. Lu, X. Chen, R. Xiong, S. Shen, C. Stachniss, and Y. Wang, "A survey on global lidar localization: Challenges, advances and open problems," *International Journal of Computer Vision*, 2024.

[5] M. Cao, X. Xu, S. Yuan, K. Cao, K. Liu, and L. Xie, "Doublebee: A hybrid aerial-ground robot with two active wheels," in *Proc. IEEE/RSJ Int. Conf. Intell. Robots Syst. (IROS)*, 2023.

[6] S. Ægidius, D. Hadjivelichkov, J. Jiao, J. Embley-Riches, and D. Kanoulas, "Watch your stepp: Semantic traversability estimation using pose projected features," in *Proc. IEEE Int. Conf. Robot. Autom. (ICRA)*, 2025.

[7] J. Lee, R. Komatsu, M. Shinozaki, T. Kitajima, H. Asama, Q. An, and A. Yamashita, "Switch-slam: Switching-based lidar-inertial-visual slam for degenerate environments," *IEEE Robot. Autom. Lett.*, 2024.

[8] N. Chen, F. Kong, W. Xu, Y. Cai, H. Li, D. He, Y. Qin, and F. Zhang, "A self-rotating, single-actuated uav with extended sensor field of view for autonomous navigation," *Science Robotics*, vol. 8, no. 76, 2023.

[9] J. Li, X. Xu, J. Liu, K. Cao, S. Yuan, and L. Xie, "Ua-mpc: Uncertainty-aware model predictive control for motorized lidar odometry," *IEEE Robot. Autom. Lett.*, 2025.

[10] J. Cui, Y. He, J. Niu, Z. Ouyang, and G. Xing, "αlidar: An adaptive high-resolution panoramic lidar system," in *Proc. Int. Conf. Mobile Comput. Netw. (MobiCom)*, 2024.

[11] Z. Zhu, Y. Fang, X. Xiao, X. Lyu, J. Mei, and B. Zhou, "Flare: Fast autonomous aerial exploration in large-scale 3d scenarios using actively rotated lidar," *IEEE Trans. Autom. Sci. Eng.*, 2025.

[12] Y. Zhang, S. Ahmadi, J. Kang, Z. Arjmandi, and G. Sohn, "Yuto mms: A comprehensive slam dataset for urban mobile mapping with tilted lidar and panoramic camera integration," *The International Journal of Robotics Research*, 2025.

[13] P. Pfreundschuh, H. Oleynikova, C. Cadena, R. Siegwart, and O. Andersson, "Coin-lio: Complementary intensity-augmented lidar-inertial odometry," in *Proc. IEEE Int. Conf. Robot. Autom. (ICRA)*, 2024.

[14] K. Xu, Z. Jiang, H. Cao, S. Yuan, C. Wang, and L. Xie, "Enhancing scene coordinate regression with efficient keypoint detection and sequential information," *IEEE Robot. Autom. Lett.*, 2025.

[15] J. Zhang, S. Singh *et al.*, "Loam: Lidar odometry and mapping in real-time." in *Robotics: Science and systems*. Berkeley, CA, 2014.

[16] X. Chen, I. Vizzo, T. Läbe, J. Behley, and C. Stachniss, "Range image-based lidar localization for autonomous vehicles," in *Proc. IEEE Int. Conf. Robot. Autom. (ICRA)*. IEEE, 2021.

[17] X. Chen, A. Milioto, E. Palazzolo, P. Giguere, J. Behley, and C. Stachniss, "Suma++: Efficient lidar-based semantic slam," in *Proc. IEEE/RSJ Int. Conf. Intell. Robots Syst. (IROS)*. IEEE, 2019.

[18] S. Chen, H. Ma, C. Jiang, B. Zhou, W. Xue, Z. Xiao, and Q. Li, "Ndt-loam: A real-time lidar odometry and mapping with weighted ndt and lfa," *IEEE Sensors Journal*, 2021.

[19] H. Wang, C. Wang, C.-L. Chen, and L. Xie, "F-loam: Fast lidar odometry and mapping," in *Proc. IEEE/RSJ Int. Conf. Intell. Robots Syst. (IROS)*. IEEE, 2021.

[20] J. Li, T.-M. Nguyen, M. Cao, S. Yuan, T.-Y. Hung, and L. Xie, "Graph optimality-aware stochastic lidar bundle adjustment with progressive spatial smoothing," *IEEE Trans. Intell. Transp. Syst.*, 2025.

[21] S. Chen, S. Yuan, T.-M. Nguyen, Z. Huang, C. Shi, J. Jing, and L. Xie, "Egs-slam: Rgb-d gaussian splatting slam with events," *IEEE Robot. Autom. Lett.*, 2025.

[22] K. Koide, M. Yokozuka, S. Oishi, and A. Banno, "Glim: 3d range-inertial localization and mapping with gpu-accelerated scan matching factors," *Robot. Auton. Syst.*, 2024.

[23] B. Lou, S. Yuan, J. Yang, W. Su, Y. Zhang, and E. Hu, "Qlio: Quantized lidar-inertial odometry," in *Proc. IEEE/RSJ Int. Conf. Intell. Robots Syst. (IROS)*, 2025.

[24] W. Xu and F. Zhang, "Fast-lio: A fast, robust lidar-inertial odometry package by tightly-coupled iterated kalman filter," *IEEE Robot. Autom. Lett.*, 2021.

[25] W. Xu, Y. Cai, D. He, J. Lin, and F. Zhang, "Fast-lio2: Fast direct lidar-inertial odometry," *IEEE Transactions on Robotics*, 2022.

[26] F. Zhu, Y. Ren, F. Kong, H. Wu, S. Liang, N. Chen, W. Xu, and F. Zhang, "Swarm-lio: Decentralized swarm lidar-inertial odometry," in *Proc. IEEE Int. Conf. Robot. Autom. (ICRA)*, 2023.

[27] Z. Chen, Y. Xu, S. Yuan, and L. Xie, "ig-lio: An incremental gicp-based tightly-coupled lidar-inertial odometry," *IEEE Robot. Autom. Lett.*, 2024.

[28] J. Lin and F. Zhang, "R3live: A robust, real-time, rgb-colored, lidar-inertial-visual tightly-coupled state estimation and mapping package," in *Proc. IEEE Int. Conf. Robot. Autom. (ICRA)*, 2022.

[29] H. Cai, S. Yuan, X. Li, J. Guo, and J. Liu, "Bev-lio(lc): Bev image assisted lidar-inertial odometry with loop closure," in *Proc. IEEE/RSJ Int. Conf. Intell. Robots Syst. (IROS)*, 2025.

[30] K. Koide, M. Yokozuka, S. Oishi, and A. Banno, "Globally consistent 3d lidar mapping with gpu-accelerated gicp matching cost factors," *IEEE Robot. Autom. Lett.*, 2021.

[31] M. Yokozuka, K. Koide, S. Oishi, and A. Banno, "Litamin2: Ultra light lidar-based slam using geometric approximation applied with kl-divergence," in *Proc. IEEE Int. Conf. Robot. Autom. (ICRA)*, 2021.

[32] C. Zhao, K. Hu, J. Xu, L. Zhao, B. Han, K. Wu, M. Tian, and S. Yuan, "Adaptive-lio: Enhancing robustness and precision through environmental adaptation in lidar inertial odometry," *IEEE Internet of Things Journal*, 2025.

[33] D. He, W. Xu, N. Chen, F. Kong, C. Yuan, and F. Zhang, "Point-lio: Robust high-bandwidth lidar-inertial odometry," *Advanced Intelligent Systems*, vol. 5, no. 7, 2023.

[34] J. Li, Z. Liu, X. Xu, J. Liu, S. Yuan, F. Xu, and L. Xie, "Limo-calib: On-site fast lidar-motor calibration for quadruped robot-based panoramic 3d sensing system," in *Proc. IEEE/RSJ Int. Conf. Intell. Robots Syst. (IROS)*, 2025.

[35] J. Li, X. Xu, Z. Liu, S. Yuan, M. Cao, and L. Xie, "Aeos: Active environment-aware optimal scanning control for uav lidar-inertial odometry in complex scenes," *ISPRS J. Photogramm. Remote Sens.*, 2026.

[36] T. Bouazza, T. Hamel, and C. Samson, "Observer design for visual–inertial estimation of pose, linear velocity and gravity direction in planar environments," *Automatica*, 2024.

[37] L. Palopoli and D. Fontanelli, "Global observability analysis of a nonholonomic robot using range sensors," in *2020 European Control Conference (ECC)*, 2020.

[38] S. Huang and R. S. H. Teo, "Geometric control of a quadrotor uav on so (3) with actuator constraints," *Unmanned Syst.*, 2025.

[39] R. Yang, Y. Qi, C. Pan, J. Wang, X. Li, H. Chen, and R. Jin, "Integrated localization method for a ground-aerial robotic system in warehouse inventory scenarios," *Unmanned Syst.*, 2025.

[40] A. Setayeshi, S. Nasrollahi, and A. Moharampour, "Terminal phase guidance law against maneuvering targets: Adaptive state-dependent differential riccati equation approach," *Unmanned Syst.*, 2025.

[41] J. Zhao, B. Duan, and J. Wang, "Adaptive impedance control for teleoperation with event-triggered controller," *Unmanned Syst.*, 2025.

[42] Y. Wang, C. Zhao, J. Liang, M. Wen, Y. Yue, and D. Wang, "Integrated localization and planning for cruise control of ugv platoons in infrastructure-free environments," *IEEE Trans. Intell. Transp. Syst.*, 2023.

[43] M. Wen, Y. Yue, Z. Wu, E. Mihankhan, and D. Wang, "Hilps: Human-in-loop policy search for mobile robot navigation," in *Proc. Int. Conf. Control Autom. Robot. Vis. (ICARCV)*. IEEE, 2020.

[44] T.-M. Nguyen, Z. Qiu, T. H. Nguyen, M. Cao, and L. Xie, "Persistently-excited adaptive relative localization and time-varying formation of robot swarms," *IEEE Transactions on Robotics*, 2019.

[45] F. Liu, S. Yuan, T.-M. Nguyen, W. Meng, and L. Xie, "Aerial target encirclement and interception with noisy range observations," *Automatica*, 2025.

[46] F. Liu, S. Yuan, K. Cao, W. Meng, and L. Xie, "Distance-based multiple noncooperative ground target encirclement for complex environments," *IEEE Trans. Control Syst. Technol.*, 2025.

[47] F. Liu, S. Yuan, W. Meng, R. Su, and L. Xie, "Multiple noncooperative targets encirclement by relative distance-based positioning and neural antisynchronization control," *IEEE Trans. Ind. Electron.*, 2024.

[48] K. Koide, M. Yokozuka, S. Oishi, and A. Banno, "Globally consistent and tightly coupled 3d lidar-inertial mapping," in *Proc. IEEE Int. Conf. Robot. Autom. (ICRA)*, 2022.

[49] J. Yin, A. Li, T. Li, W. Yu, and D. Zou, "M2dgr: A multi-sensor and multi-scenario slam dataset for ground robots," *IEEE Robotics and Automation Letters*, vol. 7, no. 2, pp. 2266–2273, 2021.

[50] D. Feng, Y. Qi, S. Zhong, Z. Chen, Q. Chen, H. Chen, J. Wu, and J. Ma, "S3e: A multi-robot multimodal dataset for collaborative slam," *IEEE Robotics and Automation Letters*, vol. 9, no. 12, pp. 11 401–11 408, 2024.

[51] P. Yin, S. Zhao, J. Wang, R. Ge, J. Ji, Y. Hu, H. Liu, and J. Han, "iloc: An adaptive, efficient, and robust visual localization system," *IEEE Transactions on Robotics*, vol. 41, pp. 2709–2726, 2025.

[52] N. Messikommer, G. Cioffi, M. Gehrig, and D. Scaramuzza, "Reinforcement learning meets visual odometry," in *European Conference on Computer Vision*. Springer, 2024.